J Mater Sci (2019) 54:671–682

Energy materials

$MoO_3/BiVO_4$ heterojunction film with oxygen vacancies for efficient and stable photoelectrochemical water oxidation

Yaqi Chen[1], Minji Yang[1], Jinyan Du[1], Gaili Ke[1], Xiaohui Zhong[1], Yong Zhou[2], Faqin Dong[1], Liang Bian[1], and Huichao He[1,*]

[1] State Key Laboratory of Environmental Friendly Energy Materials, Key Laboratory of Solid Waste Treatment and Resource Recycle of Ministry of Education, School of Materials Science and Engineering, Southwest University of Science and Technology, Mianyang 621010, China

[2] Ecomaterials and Renewable Energy Research Center, School of Physics, Nanjing University, Nanjing 211102, China

Received: 22 June 2018
Accepted: 24 August 2018
Published online: 31 August 2018

ABSTRACT

Poor charge transfer and separation rate are the major bottlenecks for the activity and stability of $BiVO_4$ photoanode. Here, we introduced oxygen vacancies into $MoO_3/BiVO_4$ heterojunction film by post-annealing the film in argon-saturated environment for improving its photoelectrochemical (PEC) water oxidation activity and stability. In comparison with the normal $MoO_3/BiVO_4$ film, the $MoO_3/BiVO_4$ film with oxygen vacancies is of better PEC water oxidation performance. Specifically, a higher photocurrent density of 4.1 mA/cm^2 in 0.1 M Na_2SO_4 at 1.1 V versus SCE was achieved on the $MoO_3/BiVO_4$ film with oxygen vacancies, which is about 200% improved over the normal $MoO_3/BiVO_4$ film (1.83 mA cm^{-2}, at 1.1 V versus SCE). In addition, the $MoO_3/BiVO_4$ film with oxygen vacancies shows more stable activity and faster kinetics for water oxidation, without significant activity loss for 5 h reaction at 1.23 V versus RHE. The enhanced performance on such a $MoO_3/BiVO_4$ film photoanode can be attributed to that the oxygen vacancies accelerate the charge transfer and separation rate between film/electrolyte interface, and thus improve the water oxidation activity and restrain the anodic photocorrosion simultaneously.

Introduction

In recent years, $BiVO_4$ has been widely studied as one of the most promising photoanode materials for photoelectrochemical (PEC) water splitting [1]. The advantages of $BiVO_4$ for PEC water splitting can be generalized as follows: First, $BiVO_4$ is of suitable band gap (~ 2.4 eV); thus, it can absorb about 11% light from the solar spectrum [2]. Second, the valence band of $BiVO_4$ is located at a more positive potential (~ 2.40 V versus RHE) than the water

Address correspondence to E-mail: hehuichao@swust.edu.cn; hehuichao2007@126.com

https://doi.org/10.1007/s10853-018-2863-6

oxidation potential (1.23 V versus RHE), allowing for solar water oxidation [3]. And third, the raw materials for the production of $BiVO_4$ photoanode are in abundance and of low cost. Under standard AM 1.5 G solar light irradiation, a theoretical photocurrent of 7.6 mA/cm^2 can be obtained on $BiVO_4$ photoanode with a high solar-to-hydrogen conversion efficiency (η_{STH}) of 9.3% [4, 5], very close to the η_{STH} of commercial requirement for PEC water splitting (10%). Unfortunately, the actual water oxidation activity on $BiVO_4$ photoanode was impeded by its poor charge transport and separation property [1, 6]. In addition, the photostability of $BiVO_4$ was suffered from anodic photocorrosion that involves the loss of V^{5+} ions from $BiVO_4$ lattice by dissolution [7]. Therefore, the modifications of $BiVO_4$ activity and stability are the forefront of PEC water splitting field.

In general, the charge transport property of $BiVO_4$ is related to its composition and morphology, and the separation property of $BiVO_4$ was affected by its surface feature. Accordingly, composition and morphology tuning are developed as two effective strategies in recent years for addressing the charge transport issue of $BiVO_4$. Typically, W and Mo co-substituting the partial sites of V in $BiVO_4$ that could improve the conductivity of $BiVO_4$ and introduce polarons into $BiVO_4$ lattice, and thus, enhanced bulk charge migration property is observed on W and Mo co-doped $BiVO_4$ photoanode [8, 9]. Furthermore, proper oxygen evolution catalysts or photocatalyst couplings have been demonstrated to be effective approaches for improving the charge separation property of $BiVO_4$. For example, FeOOH or Co-Pi (Cobalt-Phosphate) coated on $BiVO_4$ is capable of enhancing the separation of photo-generated holes and electrons on $BiVO_4$ surface [10, 11]. Owing to the matched band potentials between WO_3 and $BiVO_4$, $WO_3/BiVO_4$ heterojunction photoanode is of higher charge separation efficiency through the physical separation of surface charge [12]. On the other side, $BiVO_4$ is not thermodynamically stable enough against photocorrosion, which is the primary cause of $BiVO_4$ anodic photocorrosion. In the work of Bard et al., an inert layer of amorphous TiO_2 coupled on $BiVO_4$ film shows the function of protecting $BiVO_4$ from photocorrosion via changing the oxidation state at $BiVO_4$/electrolyte interface [13]. Additionally, Choi et al. reported the use of a V^{5+}-saturated electrolyte that can inhibit the photooxidation-coupled dissolution of $BiVO_4$ photoanode [7]. Significantly, the degree of $BiVO_4$ anodic photocorrosion critically depends on the relative rate of photocorrosion compared with the rates of interfacial charge transfer and surface charge separation [7, 10]. It reveals that when the $BiVO_4$ photoanode has faster interfacial charge transfer rate or surface charge separation rate than its photocorrosion rate, the $BiVO_4$ anodic photocorrosion can be kinetically suppressed. In summary, both the PEC activity and stability of $BiVO_4$ are determined by its charge transfer and separation properties. It is noteworthy that the reported works mainly focus on the modification of individual property of $BiVO_4$ (activity or stability), few regard to the improvements of PEC activity and stability simultaneously.

Both experimental and calculational works have revealed that oxygen vacancies can effectively modulate the electronic properties of photocatalysts, and thus improve their bulk charge transport and surface separation efficiency [14]. Normal $BiVO_4$ is of poor PEC activity due to its low carrier mobility of $\sim$ 0.044 cm^2/V s [15], while $BiVO_4$ with oxygen vacancies shows much higher PEC activity [16], indicating higher carrier mobility in $BiVO_4$ with oxygen vacancies. As remarkable charge transfer material, MoO_3 with oxygen vacancies possesses high carrier mobility up to 1100 cm^2/V s [17]. Interestingly, the band potentials between MoO_3 and $BiVO_4$ are favorable to separate the surface charge of $BiVO_4$ [18]. Inspired by this information, $MoO_3/BiVO_4$ heterojunction photoanode with oxygen vacancies is expected to have high water oxidation activity and stability. The bulk charge transport in $BiVO_4$, surface charge separation on $BiVO_4$, and the charge transfer and separation between $BiVO_4$ and MoO_3 interface all can be improved by the oxygen vacancies effect in theory.

Herein, oxygen vacancies were introduced into the $MoO_3/BiVO_4$ heterojunction film by post-annealing the film in argon-saturated environment. Subsequently, the $MoO_3/BiVO_4$ film with oxygen vacancies was investigated as photoanode for water oxidation. Due to the existence of oxygen vacancies in MoO_3 and $BiVO_4$, a high photocurrent density of 4.1 mA/cm^2 was achieved on the $MoO_3/BiVO_4$ photoanode in 0.1 M Na_2SO_4 at 1.1 V versus SCE under irradiation of simulated solar light (100 mW/cm^2). Additionally, the $MoO_3/BiVO_4$ film photoanode with oxygen vacancies shows high stability for

water oxidation, without significant loss of photoactivity for 5 h reaction.

Experimental section

Material synthesis

The $MoO_3/BiVO_4$ heterojunction film with and without oxygen vacancies was prepared using a drop-casting method on FTO glass substrate as described in our previous work with annealing modifications [18, 19]. Firstly, $Bi(NO_3)_3.5H_2O$ (Aladdin, 99.0%) was dissolved in a solvent containing concentrated HNO_3 (Aladdin, 68%) and ethylene glycol (EG, Aladdin) to form a Bi precursor solution of 25 mM. NH_4VO_3 (Sigma-Aldrich, 97%) was dissolved in EG as V precursor solution with a concentration of 25 mM. Molybdenum powder (Aladdin, 99.9%) was firstly dissolved in H_2O_2 (Aladdin, 30 wt%) and then mixed with EG to form 5 mM Mo precursor solution. Secondly, the V and Bi precursor solutions were mixed with same volume for the preparation of $BiVO_4$ film. 20 μL of mixed precursor solution was dropped on the FTO glass substrate (1.0 cm × 1.5 cm, sheet resistance < 15 Ω) that had been cleaned and sonicated with distilled water and ethanol. Next, the mixed precursor solution on FTO glass was dried at 150 °C for 60 min and then annealed at 500 °C for 120 min in air to form a $BiVO_4$ film. Finally, 10 μL of Mo precursor was dropped on the $BiVO_4$ film and then annealed at 500 °C for 120 min in air to form the $MoO_3/BiVO_4$ heterojunction film. For the introduction of oxygen vacancies, the $MoO_3/BiVO_4$ heterojunction film was further annealed at 400 °C for 40 min in an argon-saturated environment and then be marked as $MoO_3/BiVO_4$ (Ar). Based on subsequent PEC measurements, such an annealing condition was regarded as the optimal after investigating various annealing temperatures and time (temperature: 350 °C, 400 °C and 450 °C; time: 20 min, 40 min, 60 min and 100 min). For comparison, the $BiVO_4$ and MoO_3 films were treated using the same post-annealing condition in argon-saturated environment and then be marked as $BiVO_4$(Ar) and MoO_3(Ar), respectively. In addition, $MoO_3/BiVO_4(O_2)$ film was prepared via post-annealing the $MoO_3/BiVO_4$ film in O_2-saturated atmosphere at 500 °C for 2 h.

Material characterization

Scanning electron microscopy (SEM, Zeiss Supra 55 VP) and transmission electron microscope (TEM, JEOL, JEM-2010) were used to observe the morphology and microstructure of the as-prepared films. X-ray diffraction (XRD) patterns of the as-prepared films were recorded on a PANalytical X'pert PRO diffractometer equipped with Cu-Ka radiation at a scanning rate of 2°/min. Chemical state and compositions of the as-prepared films were characterized using X-ray photoelectron spectroscopy (XPS, ESCALAB 250, Thermo Scientific). UV–Vis absorption spectrum was collected on a Shimadzu UV-2600/2700 spectrophotometer. The Raman spectrum was measured using a Renishaw in Via Raman microscope with 514.5 nm argon ion laser. The electron paramagnetic resonance (EPR) measurements were taken on Bruker EMX-plus operating in the X-band (9.52 GHz) with a microwave power of 2 mW. The content of V in the electrolyte (0.1 M Na_2SO_4) that was used for PEC stability testing was measured by inductively coupled plasma technique (ICP, Thermo ICAP6300 Duo).

Electrochemical and photoelectrochemical measurements

The electrochemical and photoelectrochemical measurements were taken in a three-electrode cell (quartz cube cup, 5.0 × 5.0 × 5.0 cm^3). The as-prepared films with an area of 1.0 cm^2 were used as working electrode. The counter electrode was a Pt wire with a diameter of 0.5 mm (99.99%, CHI Instrument), and the reference electrode was saturated calomel electrode (SCE, Shanghai INESA Scientific Instrument). 0.1 M Na_2SO_4 was mainly employed as the electrolyte for electrochemical and photoelectrochemical measurements. The pH of electrolyte was checked using a benchtop pH meter (PHS-3C, Shanghai INESA Scientific Instrument). A CH Instruments 660E electrochemical workstation was used for electrochemical and photoelectrochemical measurements.

The irradiation source was a 300 W xenon lamp with AM 1.5G filter (Beijing China Education Au-light Co., Ltd.). For light measurements, the lamp was positioned to provide irradiation of 100 mW/cm^2 on the films. The light irradiation power was measured by a thermopile detector (Beijing China Education Au-light Co., Ltd.). The

photoelectrochemical measurements of the films were mainly conducted using back-side irradiation (through the FTO glass substrate to the film). IPCE measurements were taken using a full solar simulator (Beijing China Education Au-light Co., Ltd. 300 W xenon lamp) with an AM 1.5 filter and a motorized monochromator (Oriel Corner-stone 130 1/8 m). A typical monochromatic light used for the IPCE measurements can be found in Fig. S8. Light power was measured using a handheld optical power meter with a UV enhanced silicon photodetector (Newport, Models 1916C and 818-UV). The IPCE is expressed by following equation:

$$\mathrm{IPCE} = (1240 \times j)/(\lambda \times P_{\mathrm{light}}) \quad (1)$$

where j is the measured photocurrent density at a specific wavelength (mA cm^{-2}), λ is the wavelength of incident light (nm), and P_{light} is the measured light power density at that wavelength (mW/cm^2).

The electrochemical impedance spectroscopy (EIS) was performed in 0.1 M Na_2SO_4 solution under irradiation (100 mW/cm^2) at 1.23 V versus RHE with an AC amplitude of 5 mV, frequency of 10 mHz–100 kHz. Zview software was used to fit the measured EIS spectrum and get the equivalent circuit. To convert the potential (versus SCE) to RHE (NHE at pH 0), the following equation was used.

$$E_{\mathrm{RHE}} = E_{\mathrm{SCE}} + 0.0591pH + E^{\theta}_{\mathrm{SCE}} \left(E^{\theta}_{\mathrm{SCE}} = 0.2415 \text{ vs. NHE at } 25^{\circ}\mathrm{C}\right) \quad (2)$$

Mott–Schottky measurements were taken in 0.1 M Na_2SO_4 solution using an impedance versus applied potential method at a frequency of 1000 Hz. Mott–Schottky plots were created and fitted to ideal semiconductor behavior:

$$1/C^2 = \left(2/e\varepsilon\varepsilon_0 A^2 N_d\right)\left(V_a - V_{fb} - kT/e\right) \quad (3)$$

here C is the space charge layer capacitance, ε is the relative dielectric constant, ε_0 is the permittivity of free space, e is the elemental charge, A is the surface area of sample, N_d is the concentration of charge carriers, V_a is the applied potential, V_{fb} is the flat band potential, k is Boltzmann constant, and T is temperature.

To investigate whether the photocurrents on $MoO_3/BiVO_4$(Ar) film photoanode originated from the water oxidation, the Faraday efficiency of O_2 evolution [$\eta(O_2)$] was measured in a single gas-tight cell at 1.23 V versus RHE. Prior to measurement, the solution (0.1 M Na_2SO_4) was degassed by bubbling Ar for 0.5 h. The amount of generated O_2 was detected using an Agilent 7890B gas chromatograph. The value of [$\eta(O_2)$] was calculated according to Eq. (4).

$$\eta(O_2) = (\text{amount of generated } O_2) \times 100/(\text{theoretical amount of } O_2) \quad (4)$$

Titration of $KMnO_4$ solution measurement

The titration of $KMnO_4$ solution was applied to detect the quantity of H_2O_2 that formed during PEC water oxidation. Firstly, 1 mM $KMnO_4$ solution was prepared and calibrated with 1 mM $Na_2C_2O_4$ solution. Secondly, 10 mL of electrolyte (0.1 M Na_2SO_4) was collected immediately after one hour of PEC stability testing and acidified with 5 mL of 3 M H_2SO_4, and then titrated with standard $KMnO_4$ solution. Finally, the concentration of formed H_2O_2 was calculated on the basis of used volume of $KMnO_4$ standard solution. To reduce the experimental error, thrice parallel titration was carried out. The specific reaction equations related to the titration are as follows:

$$2MnO^{4-} + 5C_2O_4^{2-} + 16H^+ = 2Mn^{2+} + 10CO_2 + 8H_2O \quad (5)$$

$$2MnO^{4-} + 5H_2O_2 + 6H^+ = 2Mn^{2+} + 5O_2 + 8H_2O \quad (6)$$

Results and discussion

The morphology and microstructure of the as-prepared $BiVO_4$(Ar) and $MoO_3/BiVO_4$(Ar) film were observed using SEM and TEM. As shown in Fig. 1a, the $BiVO_4$(Ar) film is composed of randomly oriented nanoflakes and the thickness of film is about 500 nm (inset of Fig. 1a). For the $MoO_3/BiVO_4$(Ar) film, well-distributed MoO_3 nanoparticles were coupled with the $BiVO_4$ nanoflakes to form $MoO_3/BiVO_4$ heterojunctions (Fig. 1b, c). From the SEM image observation for the $MoO_3/BiVO_4$ film (shown in Fig. S1), it is found that the film is of pretty similar morphology and microstructure before and after post-annealing in argon-saturated environment. Similar observations have been found in previous works related to photocatalysts with oxygen vacancies [16]. The HRTEM image shown in Fig. 1e reveals the distance of one kind of lattice fringe to be 0.31 nm, which is

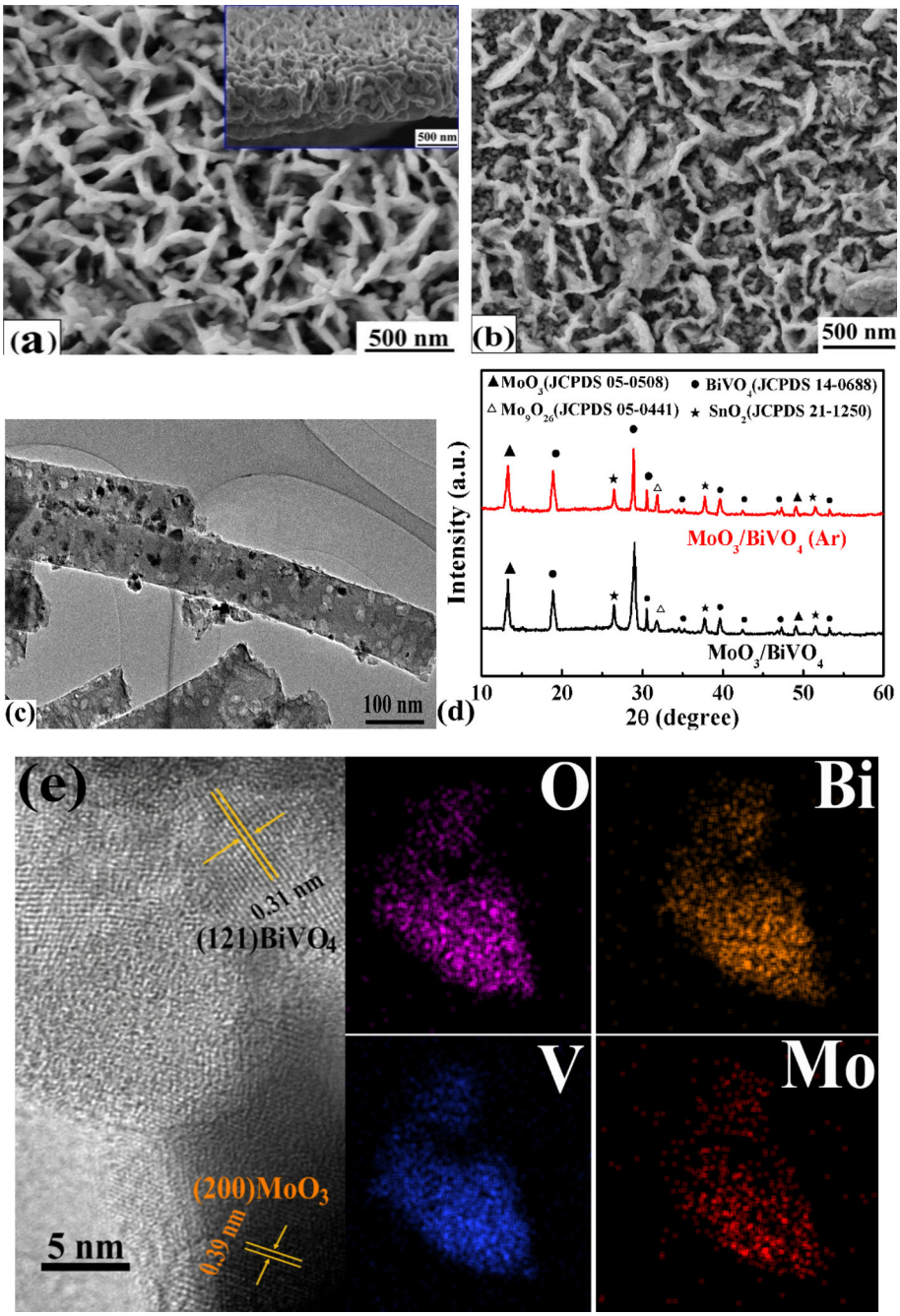

Figure 1 SEM image of **a** the $BiVO_4$(Ar) and **b** MoO_3/$BiVO_4$(Ar) film; **c** TEM image of the MoO_3/$BiVO_4$(Ar) film; **d** XRD pattern of the MoO_3/$BiVO_4$ and MoO_3/$BiVO_4$(Ar) film. **e** HRTEM image and EDS mapping of MoO_3/$BiVO_4$(Ar) film.

consistent with the interplanar spacing of the (121) planes of $BiVO_4$, and the other kind of lattice fringe to be 0.39 nm which is consistent with the interplanar spacing of the (200) planes of MoO_3. Elemental mapping shows that the MoO_3/$BiVO_4$(Ar) film possesses a homogeneous spatial distribution of Bi, V, O, and Mo species (Fig. 1e), which further confirms the successful formation of MoO_3/$BiVO_4$ heterojunctions. Figure 1d displays the X-ray diffraction (XRD) pattern of the as-prepared MoO_3/$BiVO_4$ and MoO_3/$BiVO_4$(Ar) film. As expected, the characteristic diffraction peaks of MoO_3 (JCPDS 05-0508) and $BiVO_4$ (JCPDS 14-0688) were observed in both MoO_3/$BiVO_4$ and MoO_3/$BiVO_4$(Ar) XRD patterns. In addition, a diffraction peak at 31.64° indexed to Mo_9O_{26} (JCPDS 05-0441) was observed in the XRD patterns. It is not surprising to find the characteristic diffraction peak of Mo_9O_{26} in MoO_3, because MoO_3 is a typical non-stoichiometric oxide [17, 20]. Significantly, the diffraction peak of Mo_9O_{26} is more obvious

in the XRD pattern of $MoO_3/BiVO_4$(Ar) film compared with that in the XRD pattern of $MoO_3/BiVO_4$ film, indicating higher proportion of M_9O_{26} in $MoO_3/BiVO_4$(Ar) film. Similar result was also observed in the XRD pattern of the MoO_3(Ar) film that post-annealed in argon-saturated environment (shown in Fig. S2), hinting oxygen deficit is more obvious in the post-annealed film.

The existence of oxygen vacancies in $MoO_3/BiVO_4$(Ar) film was characterized by Raman, XPS and EPR technique. In the Raman spectra (Fig. 2a), the peak around 210 cm^{-1} is attributed to the external mode of $BiVO_4$, while the peaks around 330 and 365 cm^{-1} are assigned to the asymmetric and symmetric deformation modes of the VO_4^{3-} tetrahedron ($\delta_{as}(VO_4^{3-})$ and $\delta_s(VO_4^{3-})$), respectively [21]. Furthermore, a peak around 825 cm^{-1} was observed, which corresponds to anti-symmetric stretching of V-O. It is noteworthy that the peak location of anti-symmetric V-O stretching for $MoO_3/BiVO_4$(Ar) film was shifted to higher wave number (825 cm^{-1}) relative to the $MoO_3/BiVO_4$ film (823 cm^{-1}). In the previous reports related to $BiVO_4$ with oxygen vacancies, similar change on the peak of anti-symmetric V-O stretching was observed [16, 22], suggesting the existence of oxygen vacancies in $MoO_3/BiVO_4$(Ar) film. Additionally, the Bi 4f and V 2p peaks in the XPS spectrum of $MoO_3/BiVO_4$(Ar) film both show shift to lower binding energy compared with those in $MoO_3/BiVO_4$ film (Fig. 2b, c). Such changes can be attributed to the introduction of oxygen vacancies that results in partial reduction of Bi^{3+} and V^{5+} ions. [14] Simultaneously, a shift of the Mo 3d peaks to lower binding energy was observed in the XPS spectrum of $MoO_3/BiVO_4$(Ar) film (Fig. 2d), confirming the presence of oxygen vacancies in MoO_3. Furthermore, the $MoO_3/BiVO_4$(Ar) film was further characterized by EPR spectroscopy to detect the presence of oxygen vacancies in the film. As recorded in Fig. 2e, the EPR spectrum for $MoO_3/BiVO_4$ film and $MoO_3/BiVO_4$ (Ar) film both shows a signal center at g = 1.978, which is consisted to the g value for paramagnetic V^{4+} [23].

However, the EPR signal of $MoO_3/BiVO_4$ (Ar) film shows markedly increased than that of $MoO_3/BiVO_4$ film, confirming the presence of oxygen defects in $MoO_3/BiVO_4$(Ar) film [24]. According to the XRD patterns, Raman, XPS and EPR spectrum, we can conclude that the oxygen vacancies were successfully introduced into $MoO_3/BiVO_4$ film by post-annealing the film in argon-saturated atmosphere.

To optimize the PEC activity of $MoO_3/BiVO_4$(Ar) film, different post-annealing temperatures and time were investigated in the argon-saturated atmosphere. The LSV measurements indicate that the $MoO_3/BiVO_4$ film post-annealed at 400 °C for 40 min in argon-saturated atmosphere is of the optimal PEC water oxidation activity (shown in Fig. S3a and S3b). Thus, this post-annealing condition was used to treat the $MoO_3/BiVO_4$ film for subsequent investigation.

Figure 3a, b shows the LSV and i-t curves of the $MoO_3/BiVO_4$ film with and without oxygen vacancies that measured in 0.1 M Na_2SO_4 under AM 1.5G irradiation. Both under front and back irradiation, the $MoO_3/BiVO_4$(Ar) film shows enhanced photocurrent density. A higher photocurrent density of 4.10 mA cm^{-2} is achieved on the $MoO_3/BiVO_4$(Ar) under back irradiation at 1.1 V versus SCE, which is over 200% enhancement compared with the $MoO_3/BiVO_4$ film (1.83 mA cm^{-2}) at the same condition. The Faraday efficiency of O_2 evolution on $MoO_3/BiVO_4$(Ar) film electrode is close to 100%, indicating that the photocurrent on the film is mainly originated from the PEC water oxidation (shown in Fig. S4). In addition, the onset potential of photocurrent was negatively shifted on the $MoO_3/BiVO_4$(Ar) film (0.03 V versus SCE) compared with the $MoO_3/BiVO_4$ film (0.23 V versus SCE), revealing its faster water oxidation kinetics. For comparison and confirmation, the PEC water oxidation activity on $MoO_3/BiVO_4$ (O_2) film that was prepared via post-annealing the $MoO_3/BiVO_4$ film in O_2 atmosphere at 500 °C for 2 h was investigated. In general, the $MoO_3/BiVO_4(O_2)$ film is of similar activity as the $MoO_3/BiVO_4$ film (see in Fig. S3d), both lower than that of the $MoO_3/BiVO_4$(Ar) film. Besides, higher photocurrent was observed on the MoO_3 and $BiVO_4$ film with oxygen vacancies (Fig. S5), further demonstrating the positive effect of oxygen vacancies on the water oxidation activity of photoanode. To clarify the role of oxygen vacancies, the charge separation and injection efficiency of $MoO_3/BiVO_4$(Ar) and $MoO_3/BiVO_4$ film were quantificationally evaluated based on the LSV measurements in a hole scavenger (Na_2SO_3) containing solution (see Fig. S6) and the absorbed photon flux of films (see Fig. 5c). In comparison with the $MoO_3/BiVO_4$ film, higher charge separation and injection efficiency were achieved on the $MoO_3/BiVO_4$(Ar) film (Fig. 3c, d). The charge separation

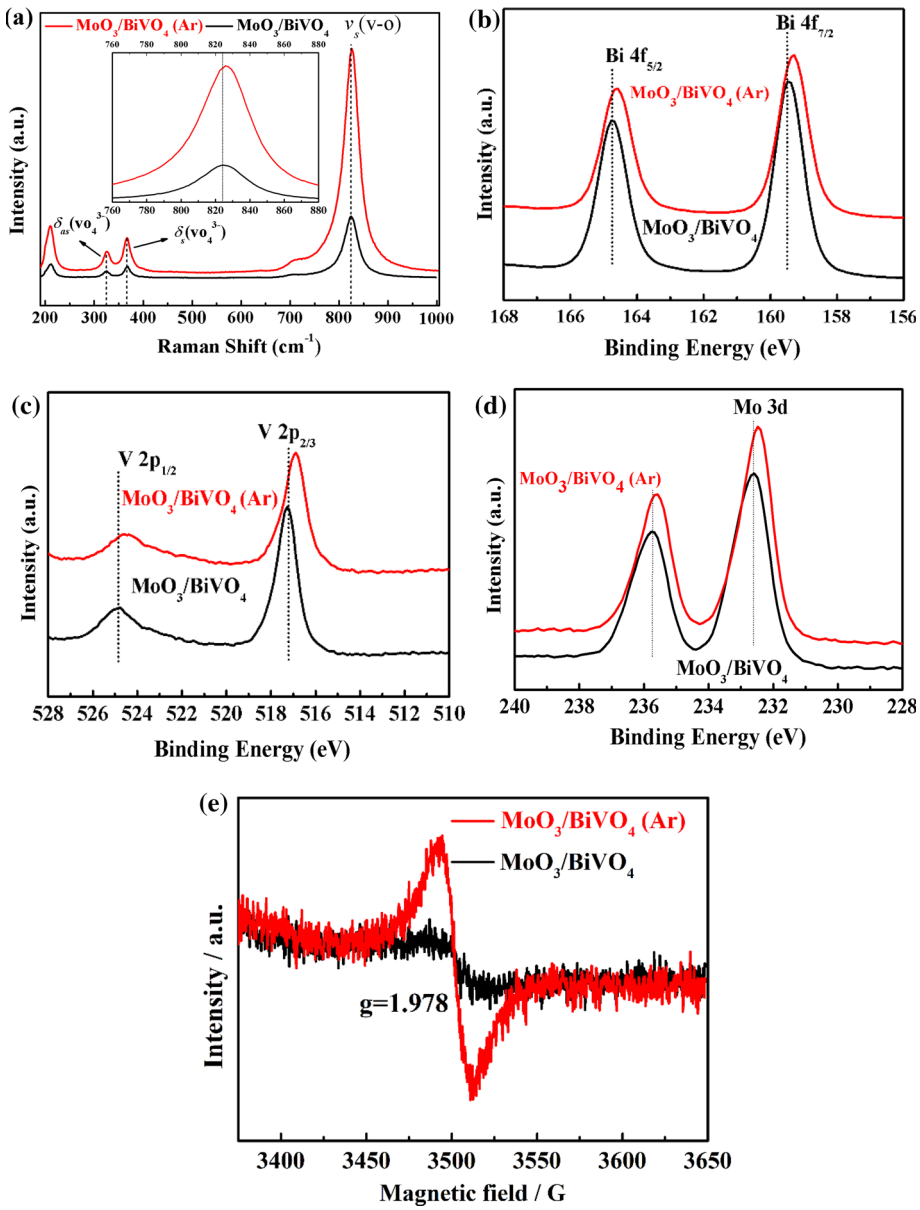

Figure 2 **a** Raman spectra of the $MoO_3/BiVO_4$ and $MoO_3/BiVO_4$(Ar) film. High-resolution XPS spectra of the **b** Bi 4f, **c** V 2p and **d** Mo 3d obtained from the $MoO_3/BiVO_4$ and $MoO_3/BiVO_4$(Ar) film. **e** EPR spectra of the $MoO_3/BiVO_4$ and $MoO_3/BiVO_4$(Ar) film.

and injection efficiency on the $MoO_3/BiVO_4$(Ar) film are, respectively, 34.5% and 72.0% at 1.23 V versus RHE, while those on the $MoO_3/BiVO_4$ film are 30.0% (separation efficiency) and 46.0% (injection efficiency), respectively. It is generally accepted that the charge-injection efficiency of photoanode is related to its surface reaction kinetics. Comparatively speaking, the charge-injection efficiency for the $MoO_3/BiVO_4$ film with oxygen vacancies is particularly improved, indicating that the oxygen vacancies have more obvious influence on the water oxidation kinetics of $MoO_3/BiVO_4$ film.

The influence of oxygen vacancies on the PEC water oxidation kinetics of $MoO_3/BiVO_4$ photoanode was investigated by electrochemical impedance spectroscopy (EIS). As shown in Fig. 4a, two slightly depressed semicircles are observed in the Nyquist plots that measured on the $MoO_3/BiVO_4$ and $MoO_3/BiVO_4$(Ar) film electrode under irradiation. It is well known that the arc of semicircle in this typical Nyquist plot is relevant to the charge separation and transfer kinetics at electrode/electrolyte interface [25]. The semicircle arcs of $MoO_3/BiVO_4$ (Ar) film electrode are much smaller than those of $MoO_3/BiVO_4$ film electrode, suggesting faster charge separation and transfer kinetics during PEC water oxidation. The equivalent circuit in the light of measured impedance data was shown in Fig. 4b. In the

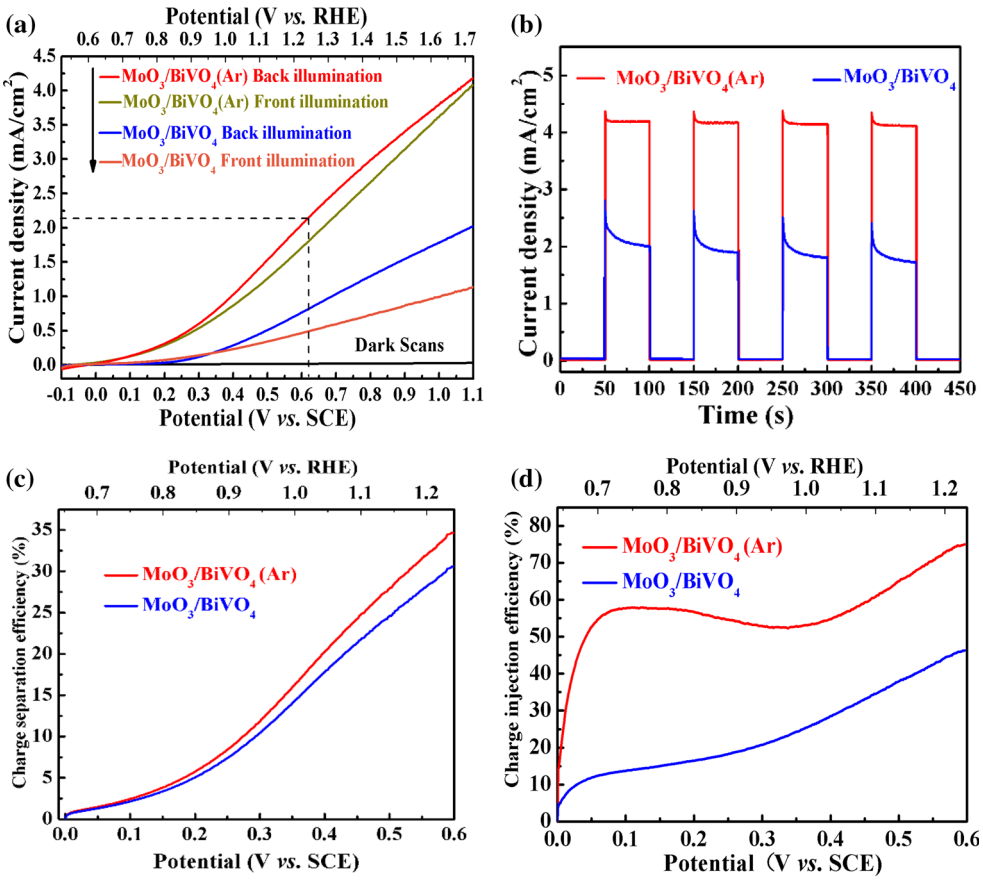

Figure 3 **a** LSV scans and **b** amperometric i-t curves for the $MoO_3/BiVO_4$ and $MoO_3/BiVO_4$(Ar) film in 0.1 M Na_2SO_4 under illumination with 100 mW/cm^2 simulated solar light. Calculated charge separation **c** and injection **d** efficiency of $MoO_3/BiVO_4$ and $MoO_3/BiVO_4$(Ar) film.

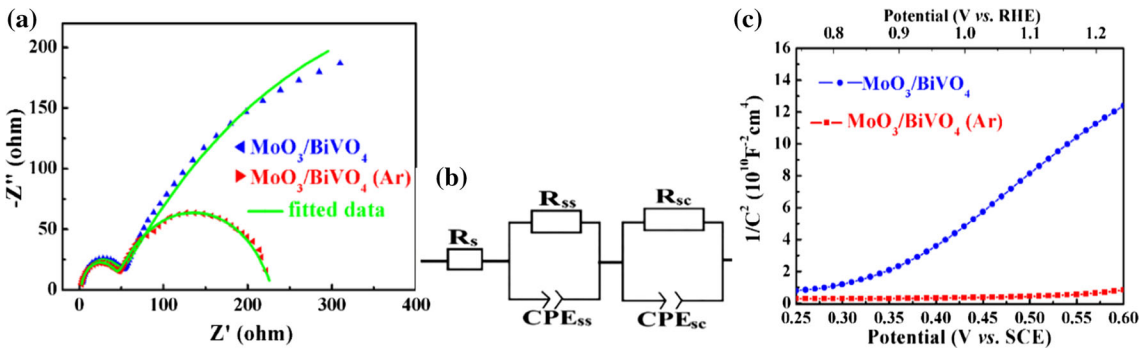

Figure 4 **a** Nyquist plots of the $MoO_3/BiVO_4$ and $MoO_3/BiVO_4$(Ar) film electrode. The EIS measurements were performed in 0.1 M Na_2SO_4 at 1.23 V versus RHE under 100 mW/cm^2 simulated solar light illumination. The solid line in Fig. 4a is the fitted data from Zview software using the proposed equivalent circuit model. **b** An equivalent circuit for the film electrode. **c** Mott–Schottky plots for the $MoO_3/BiVO_4$ and $MoO_3/BiVO_4$(Ar) film electrode in 0.1 M Na_2SO_4 at a frequency of 1000 Hz under AM 1.5G illumination.

equivalent circuit, *R*s represents the resistance of solution, *R*ss is the surface state resistance related to the charge transfer from the valence band or conduction band to the surface of semiconductor electrode [25], *R*sc is the space charge separation resistance [18], and *CPE*ss and *CPE*sc are the constant phase elements for the electrolyte/electrode interface and electrode surface, respectively. The fitted values of *R*sc and *R*ss for the $MoO_3/BiVO_4$(Ar) film electrode are 30.45 Ω and 186.5 Ω, respectively, which are much lower than those for the $MoO_3/BiVO_4$ film electrode (*R*sc: 49.21Ω; *R*ss: 894.9Ω, shown in Table 1). The EIS result demonstrates that the $MoO_3/BiVO_4$ film with oxygen vacancies has faster interfacial

charge transfer and separation rate during PEC water oxidation. Figure 4c shows the Mott–Schottky plots for the $MoO_3/BiVO_4$ and $MoO_3/BiVO_4$(Ar) film electrode in 0.1 M Na_2SO_4 under 100 mW/cm^2 simulated solar light irradiation. Positive slope was observed in the Mott–Schottky plots for both $MoO_3/BiVO_4$ and $MoO_3/BiVO_4$(Ar) film electrode, showing typical feature of n-type semiconductor. In comparison with the $MoO_3/BiVO_4$ film electrode, the $MoO_3/BiVO_4$(Ar) film electrode shows a lower slope in its Mott–Schottky plot. From the SEM observations, we know that the $MoO_3/BiVO_4$ film both with and without oxygen vacancies has similar morphology and microstructure (see Fig. S1). Under the same measurement conditions, the slope of Mott–Schottky plot is inversely proportional to the charge carrier density of film electrode (see the Mott–Schottky equation in *Experimental section*) [26, 27]. Accordingly, it can infer that the $MoO_3/BiVO_4$ film with oxygen vacancies is of higher charge density than the normal $MoO_3/BiVO_4$ film under irradiation.

The above results suggest that the introduction of oxygen vacancies improves the PEC water oxidation activity of $MoO_3/BiVO_4$ film obviously. To investigate the relation between the PEC activity and the wavelength of the incident light quantitatively, incident photon-to-current conversion efficiency (IPCE) measurements were taken for the films. Figure 5a is the IPCE spectrum for the $MoO_3/BiVO_4$ and $MoO_3/BiVO_4$(Ar) film that measured in 0.1 M Na_2SO_4 at 1.23 V versus RHE. For both the $MoO_3/BiVO_4$ and $MoO_3/BiVO_4$(Ar) films, the photoresponse ranges are observed from 320 to 520 nm, which are consistent with their UV–Vis absorption spectrum (Fig. 5b). However, the $MoO_3/BiVO_4$(Ar) shows higher IPCE than the $MoO_3/BiVO_4$ film, further confirming their PEC activity difference. The photocurrent density of $MoO_3/BiVO_4$ and $MoO_3/BiVO_4$(Ar) film was, respectively, integrated to 0.78 mA/cm^2 and 2.02 mA/cm^2 using their IPCE spectrum data, which are close to the photocurrent value from their LSV results (the data shown in Table S1). Significantly, the $MoO_3/BiVO_4$ film has similar optical absorption behavior regardless of oxygen vacancies (Fig. 5b). Based on the absorbed photon flux spectra (Fig. 5c), the total absorbed photocurrents of $MoO_3/BiVO_4$ and $MoO_3/BiVO_4$(Ar) film are integrated to be 5.91 mA cm^{-2} and 6.01 mA cm^{-2}, respectively. Combined with the PEC activity results and optical absorption spectra, it can be concluded that the dramatically enhanced PEC water oxidation activity on $MoO_3/BiVO_4$(Ar) film cannot be caused by the slight difference of light absorption.

For the water oxidation on photoanode, the stability is an important parameter to estimate the performance of photoanode. Figure 6a shows the PEC stability curve of the $MoO_3/BiVO_4$ and $MoO_3/BiVO_4$(Ar) film in 0.1 M Na_2SO_4 at 1.23 V versus RHE. For the $MoO_3/BiVO_4$ film, the photocurrent density drops from 0.63 mA cm^{-2} to 0.14 mA cm^{-2} after 10000 s of irradiation. The PEC activity decay of $MoO_3/BiVO_4$ film is mainly ascribed to the anodic photocorrosion that originated from the photooxidation-coupled dissolution of V^{5+} on the $BiVO_4$ film. As a contrast, stable photocurrent ($\sim$ 2.0 mA cm^{-2}) was obtained on the $MoO_3/BiVO_4$(Ar) film under a longer irradiation time of 18000 s. It is necessary to point out that the PEC activity on $MoO_3/BiVO_4$ (Ar) film shows decreased trend when in excess of 5 h reaction. However, about 90% PEC activity can be recovered by re-annealing the $MoO_3/BiVO_4$ (Ar) film at 400 °C for 40 min in argon-saturated atmosphere ($MoO_3/BiVO_4$ (Ar) 2nd cycle in Fig. 6a). After the PEC stability testing, the concentration of V in Na_2SO_4 solution which was used as electrolyte for PEC stability testing was detected by ICP technique. As shown in Table 2, the concentration of V is 3.28 μM in the Na_2SO_4 solution which was used for the $MoO_3/BiVO_4$ film stability testing, confirming that the attenuation of PEC activity is initiated by V^{5+} dissolving. A lower V concentration of 0.90 μM was detected in the $MoO_3/BiVO_4$(Ar) film that used Na_2SO_4 solution. Additionally, we further detected the concentration of H_2O_2 that may be formed

Table 1 The values of the elements in equivalent circuit fitted in the Nyquist plots of Fig. 4a

Sample	Rs/Ω (Error/%)	Rsc/Ω (Error/%)	CPEsc-P (Error/%)	CPEsc-T/F (Error/%)	Rss/Ω (Error/%)	CPEss-P (Error/%)	CPEss-T/F (Error/%)
$MoO_3/BiVO_4$	2.023 (4.32)	49.21 (3.93)	2.47E−4 (2.33)	3.494E−7 (4.12)	894.9 (2.54)	0.6115 (1.81)	2.102E−4 (5.45)
$MoO_3/BiVO_4$(Ar)	2.0324 (3.67)	30.45 (1.32)	3.72E−4 (1.67)	4.587E−7 (3.51)	186.5 (1.25)	0.7619 (1.10)	9.478E−5 (4.88)

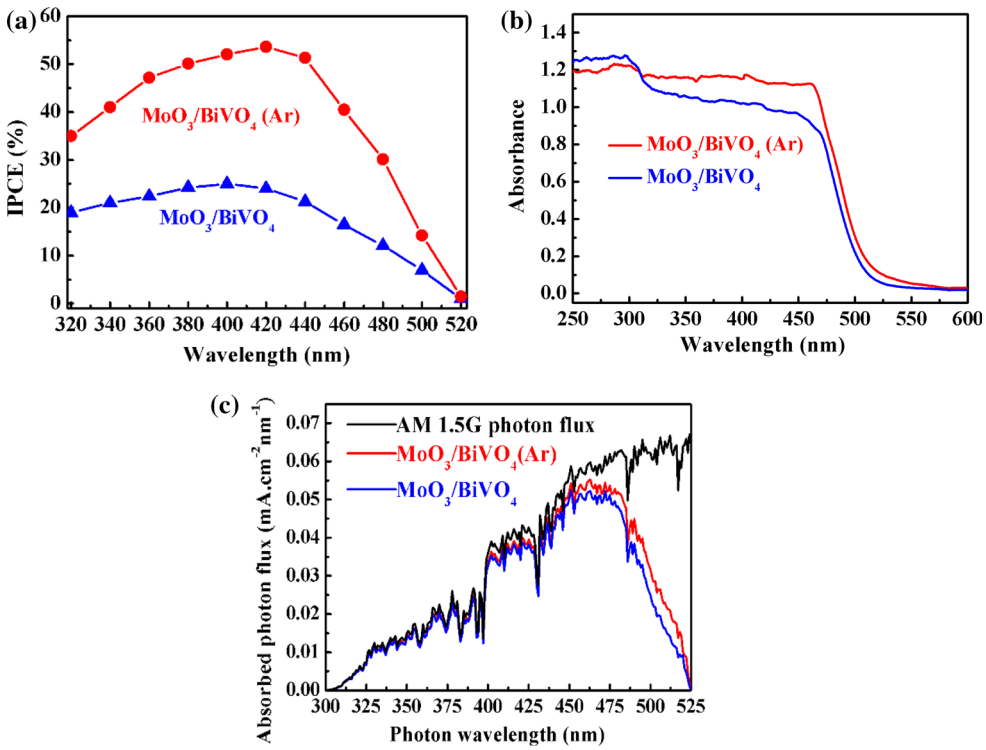

Figure 5 **a** IPCE spectra of the $MoO_3/BiVO_4$ and $MoO_3/BiVO_4$(Ar) film in 0.1 M Na_2SO_4 at 1.23 V versus RHE. **b** UV–Vis absorbance spectra and **c** absorbed photon flux of the $MoO_3/BiVO_4$ and $MoO_3/BiVO_4$(Ar) film.

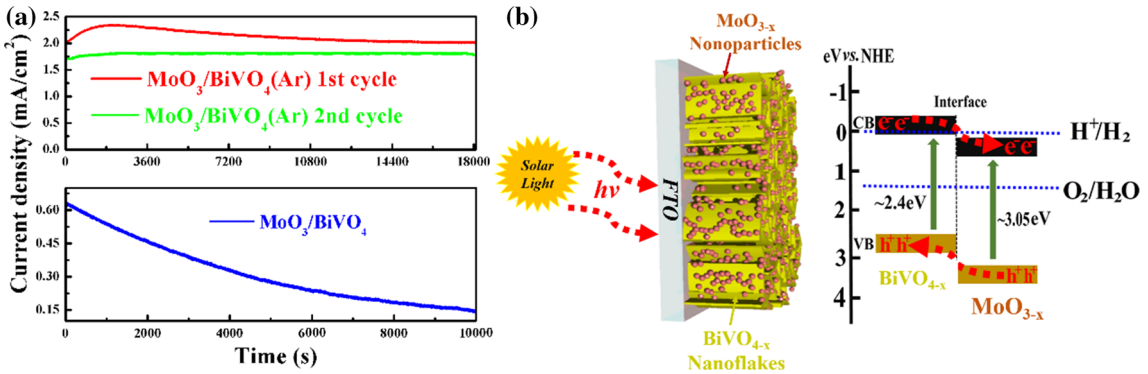

Figure 6 **a** Photocurrent density versus time curves for the $MoO_3/BiVO_4$ and $MoO_3/BiVO_4$(Ar) film in 0.1 M Na_2SO_4 at 1.23 V versus RHE. **b** Schematics of charge transfer and separation on the $MoO_3/BiVO_4$ (Ar) film.

through a two-electron pathway on the films during PEC stability testing [28]. After 3600 s of PEC stability testing, 10 mL of 0.1 M Na_2SO_4 electrolyte was sampled immediately for $KMnO_4$ titration to detect the concentration of H_2O_2. The concentration of H_2O_2 from the electrolyte that was used for $MoO_3/BiVO_4$ film PEC stability testing is 6.53 μM, and for the $MoO_3/BiVO_4$(Ar) film is 2.24 μM (Table 3), revealing weaker H_2O_2 formation on the $MoO_3/BiVO_4$(Ar) film and thus weaker anodic photocorrosion. Actually, the anodic photocorrosion rate of $BiVO_4$ was influenced by its interfacial charge transfer and surface recombination rate [7, 10]. The degree of $BiVO_4$ anodic photocorrosion can be kinetically suppressed through the improvement of its interfacial charge transfer rate. Combined with PEC results above (the charge separation and injection efficiency and EIS), it can be reasonably inferred that the $MoO_3/BiVO_4$ film

Table 2 The ICP results of dissolved concentration of V in 0.1 M Na_2SO_4 that used for stability testing of the films

Sample	Concentration of V (μM)
$MoO_3/BiVO_4$	3.28
$MoO_3/BiVO_4$(Ar)	0.90

Table 3 The formed concentration of H_2O_2 in 0.1 M Na_2SO_4 that used for PEC stability testing of the films

Sample	Concentration of H_2O_2 (μM)
$MoO_3/BiVO_4$	6.53
$MoO_3/BiVO_4$(Ar)	2.24

with oxygen vacancies is capable of restraining the anodic photocorrosion of $BiVO_4$, because of its improved interfacial charge transfer and surface charge separation rate.

The flat band potential of MoO_3(Ar) and $BiVO_4$(Ar) was, respectively, determined to be 0.56 V versus RHE and 0.06 V versus RHE by Mott–Schottky measurement (shown in Fig.S7a and 7b). Based on the semi-empirical theory that the conduction band potential of n-type semiconductors is often more negative by about 0.1 V than its flat band potential [29], the conduction band potential of MoO_3(Ar) and $BiVO_4$(Ar) is inferred to be 0.46 V versus RHE and -0.04 V versus RHE, respectively. Meanwhile, the band gap of MoO_3(Ar) film is determined to be 3.05 eV (see Fig.S7c and 7d). On the basis of results obtained above, a possible mechanism for the improved PEC water oxidation performance on the $MoO_3/BiVO_4$(Ar) film was proposed (Fig. 6b). For the $MoO_3/BiVO_4$ film with oxygen vacancies, effective heterojunctions are formed at $MoO_{3-x}/BiVO_{4-x}$ interface through their physical coupling and band potentials matching. Under irradiation with solar light, the photo-generated electrons and holes on $BiVO_{4-x}$ surface are orderly separated and transferred. Specifically, the electrons on $BiVO_4$ surface are transferred to MoO_3 due to the conduction band potential difference between $BiVO_4$ and MoO_3, while the holes physically stayed on $BiVO_4$ for driving the water oxidation reaction. Duo to the presence of oxygen vacancies in MoO_3 and $BiVO_4$, the interfacial charge transfer and separation rate were accelerated. As a result, the PEC water oxidation activity on $MoO_3/BiVO_4$(Ar) film was improved as well as the anodic photocorrosion was restrained.

Conclusions

In summary, oxygen vacancies were introduced into the $MoO_3/BiVO_4$ film photoanode to improve its PEC water oxidation activity and stability. In comparison with $MoO_3/BiVO_4$ film, a higher photocurrent density of 4.1 mA/cm^2 was achieved on the $MoO_3/BiVO_4$ film with oxygen vacancies at 1.1 V versus SCE in 0.1 M Na_2SO_4. In addition, the $MoO_3/BiVO_4$ photoanode with oxygen vacancies shows higher water oxidation stability, without significant loss of photoactivity for 5 h reaction. The enhanced performance on such a $MoO_3/BiVO_4$ film can be attributed to that the oxygen vacancies accelerate the charge transfer and separation rate between film/electrolyte interface and thus improve the PEC water oxidation activity and restrain the anodic photocorrosion.

Acknowledgements

The authors acknowledge National Basic Research Program of China (973 Program: 2014CB846003), National Natural Science Foundation of China (41702037), Sichuan Science and Technology Program (2017JY0146 and 2018JY0462), Research Fund of Southwest University of Science and Technology (15zx7104 and 15zx7123).

Compliance with ethical standards

Conflicts of interest The authors declare that they have no conflicts of interest.

Electronic supplementary material: The online version of this article (https://doi.org/10.1007/s10853-018-2863-6) contains supplementary material, which is available to authorized users.

References

[1] Tan HL, Amal R, Ng YH (2017) Alternative strategies in improving the photocatalytic and photoelectrochemical activities of visible light-driven $BiVO_4$: a review. J Mater Chem A 5:16498–16521

[2] Jia Q, Iwashina K, Kudo A (2012) Facile fabrication of an efficient $BiVO_4$ thin film electrode for water splitting under visible light irradiation. Proc Natl Acad Sci 109:11564–11569

[3] Walsh A, Yan Y, Huda MN, Al-Jassim MM, Wei SH (2009) Band edge electronic structure of $BiVO_4$: elucidating the role of the bis and Vd orbitals. Chem Mater 21:547–551

[4] Kim TW, Choi KS (2014) Nanoporous $BiVO_4$ photoanodes with dual-layer oxygen evolution catalysts for solar water splitting. Science 343:990–994

[5] Chen Z, Jaramillo TF, Deutsch TG, Kleiman-Shwarsctein A, Forman AJ, Gaillard N, Garland R, Takanabe K, Heske C, Sunkara M (2010) Accelerating materials development for photoelectrochemical hydrogen production: standards for methods, definitions, and reporting protocols. J Mater Res 25:3–16

[6] Zhao Z, Li Z, Zou Z (2011) Electronic structure and optical properties of monoclinic clinobisvanite $BiVO_4$. Phys Chem Chem Phys 13:4746–4753

[7] Lee DK, Choi KS (2018) Enhancing long-term photostability of $BiVO_4$ photoanodes for solar water splitting by tuning electrolyte composition. Nat Energy 3:53–60

[8] Park HS, Kweon KE, Ye H, Paek E, Hwang GS, Bard AJ (2011) Factors in the metal doping of $BiVO_4$ for improved photoelectrocatalytic activity as studied by scanning electrochemical microscopy and first-principles density-functional calculation. J Phys Chem C 115:17870–17879

[9] Luo W, Yang Z, Li Z, Zhang J, Liu J, Zhao Z, Wang Z, Yan S, Yu T, Zou Z (2012) Solar hydrogen generation from seawater with a modified $BiVO_4$ photoanode. Energy Environ Sci 4:4046–4051

[10] Seabold JA, Choi KS (2012) Efficient and stable photo-oxidation of water by a bismuth vanadate photoanode coupled with an iron oxyhydroxide oxygen evolution catalyst. J Am Chem Soc 134:2186–2192

[11] Abdi FF, Krol R (2012) Nature and light dependence of bulk recombination in Co-Pi catalyzed $BiVO_4$ photoanodes. J Phys Chem C 116:9398–9404

[12] Rao PM, Cai L, Liu C, Cho IS, Lee CH, Weisse JM, Yang P, Zheng X (2014) Simultaneously efficient light absorption and charge separation in $WO_3/BiVO_4$ core/shell nanowire photoanode for photoelectrochemical water oxidation. Nano Lett 14:1099–1105

[13] Eisenberg D, Ahn HS, Bard AJ (2014) Enhanced photoelectrochemical water oxidation on bismuth vanadate by electrodeposition of amorphous titanium dioxide. J Am Chem Soc 136:14011–14014

[14] Wang G, Yang Y, Han D, Li Y (2017) Oxygen defective metal oxides for energy conversion and storage. Nano Today 13:23–39

[15] Abdi FF, Savenije TJ, May MM, Dam B, van de Krol R (2013) The origin of slow carrier transport in $BiVO_4$ thin film photoanodes: a time-resolved microwave conductivity study. J Phys Chem Lett 4:2752–2757

[16] Wu JM, Chen Y, Pan L, Wang P, Cui Y, Kong DC, Wang L, Zhang X, Zou JJ (2018) Multi-layer monoclinic $BiVO_4$ with oxygen vacancies and V^{4+} species for highly efficient visible-light photoelectrochemical applications. Appli Catal B Environ 221:187–195

[17] Balendhran S, Deng J, Ou JZ, Walia S, Scott J, Tang J, Wang KL, Field MR, Russo S, Zhuiykov S, Strano MS, Medhekar N, Sriram S, Bhaskaran M, Kalantar-zadeh K (2013) Enhanced charge carrier mobility in two-dimensional high dielectric molybdenum oxide. Adv Mater 25:109–114

[18] He H, Zhou Y, Ke G, Zhong X, Yang M, Bian L, Lv K, Dong F (2017) Improved surface charge transfer in $MoO_3/BiVO_4$ heterojunction film for photoelectrochemical water oxidation. Electrochim Acta 257:181–191

[19] He H, Berglund SP, Rettie A, Chemelewski W, Xiao P, Zhang Y, Mullins CB (2017) Synthesis of $BiVO_4$ nanoflake array films for photoelectrochemical water oxidation. J Mater Chem A 24:9371–9379

[20] Bouzidi A, Benramdane N, Tabet-Derraz H, Mathieu C, Khelifa B, Desfeux R (2003) Effect of substrate temperature on the structural and optical properties of MoO_3 thin films prepared by spray pyrolysis technique. Mater Sci Eng, B 97:5–8

[21] Yoon H, Mali MG, Choi JY, Kim MW, Choi SK, Park H, Al-Deyab SS, Swihart MT, Yarin AL, Yoon SS (2015) Nanotextured pillars of electrosprayed bismuth vanadate for efficient photoelectrochemical water splitting. Langmuir 31:3727–3737

[22] Tan H, Suyanto A, De Denko AT, Saputera WH, Amal R, Osterloh FE, Ng Y (2017) Enhancing the photoactivity of faceted $BiVO_4$ via annealing in oxygen-deficient condition. Part Part Syst Charact 34:1600290

[23] Zapart MB, Zapart W, Wyslocki B, Zhukov AP (1988) EPR of V^{4+} ions in $SbVO_4$. Ferroelectrics 80:55–58

[24] Zheng JY, Lyu HY, Xie C, Wang RL, Tao L, Wu HB, Zhou HJ, Jiang SP, Wang SY (2018) Defect-enhanced charge separation and transfer within protection layer/semiconductor structure of photoanodes. Adv Mater 30:1801773

[25] Bohra D, Smith WA (2015) Improved charge separation via Fe-doping of copper tungstate photoanodes. Phys Chem Chem Phys 17:9857–9866

[26] Parmar KPS, Kang HJ, Bist A, Dua P, Jang JS, Lee JS (2012) Photocatalytic and photoelectrochemical water oxidation over metal-doped monoclinic BiVO4 photoanodes. Chemsuschem 5:1926–1934

[27] Ma M, Zhang K, Li P, Jung MS, Jeong MJ, Park JH (2016) Dual oxygen and tungsten vacancies on a WO_3 photoanode for enhanced water oxidation. Angew Chem Int Ed 128:11998–12002

[28] Fuku K, Miyase Y, Miseki Y, Funaki T, Gunji T, Sayama K (2017) Photoelectrochemical hydrogen peroxide production from water on a $WO_3/BiVO_4$ photoanode and from O_2 on an Au cathode without external bias. Chem Asian J 12:1111–1119

[29] Matsumoto Y, Omae M, Sato E, Watanabe I (1986) Photoelectrochemical properties of the Zn-Ti-Fe spinel oxides. J Electrochem Soc 133:711–716